Sustainable Energy & Fuels

Vapor-Fed Photoelectrolysis of Water at 0.3 V Using Gas-Diffusion Photoanodes of SrTiO3 Layers

Journal:	*Sustainable Energy & Fuels*
Manuscript ID	SE-ART-11-2019-001068.R1
Article Type:	Paper
Date Submitted by the Author:	28-Oct-2019
Complete List of Authors:	Amano, Fumiaki; The University of Kitakyushu, Department of Chemical and Environmental Engineering Mukohara, Hyosuke; The University of Kitakyushu, Department of Chemical and Environmental Engineering Sato, Hiroki; The University of Kitakyushu, Department of Chemical and Environmental Engineering Tateishi, Chihiro; The University of Kitakyushu, Department of Chemical and Environmental Engineering Sato, Hiromasa; Institute for Molecular Science, 杉本, 敏樹; Institute for Molecular Science, ; JST,

ARTICLE

Vapor-Fed Photoelectrolysis of Water at 0.3 V Using Gas-Diffusion Photoanodes of $SrTiO_3$ Layers

Received 00th January 20xx,
Accepted 00th January 20xx

DOI: 10.1039/x0xx00000x

Fumiaki Amano,*[ab] Hyosuke Mukohara,[a] Hiroki Sato,[a] Chihiro Tateishi,[a] Hiromasa Sato,[c] and Toshiki Sugimoto[bc]

Large scale production of H_2 using renewable energies can be realized by photoelectrochemical (PEC) splitting of water vapor in the gas phase. Air humidity can be a water resource for producing solar H_2. The concept is based on photoelectrochemistry under a gas environment using a proton exchange membrane (PEM) as a solid polymer electrolyte and a macroporous semiconductor electrode wrapped in a perfluorosulfonic acid ionomer. A prototype vapor-fed PEC cell using TiO_2 gas-diffusion electrodes as an O_2-evolving photoanode and a carbon-supported platinum catalyst cathode showed water splitting to evolve O_2 and H_2, which are physically separated from each other by the PEM. Herein, we demonstrate a PEM-PEC system consisting of a strontium titanate ($SrTiO_3$) nanocrystalline layer decorated on a titanium microfiber felt to achieve overall water splitting into H_2 and O_2 at a ratio of 2:1 on each electrode at an applied voltage of only 0.3 V under the gaseous condition. In comparison with TiO_2 electrodes, the $SrTiO_3$ gas-diffusion electrode decreased the external voltage and suppressed the gradual decomposition of the ionomer coated on the photoanode. These differences are because of the cathodic shift of the photocurrent onset potential and improvement of the Faraday efficiency of O_2 evolution, respectively. The interface between the $SrTiO_3$ surface and the ionomer thin film exhibited fast kinetics for O_2 evolution from water adsorbates supplied from the gas phase and durability under ultraviolet light irradiation.

Introduction

Using sunlight as an alternative energy resource is a challenge for solving the environmental problems related carbon dioxide (CO_2) emission that will be encountered in the near future.[1] The conversion of solar power to energy carriers, which can be stored and transported for later use, is necessary to mitigate the inherent intermittencies.[2, 3] Hydrogen (H_2) is the simplest energy carrier, which is produced from water and can be efficiently used by fuel cell technologies. However, solar H_2 production faces a problem in the cost of photovoltaic power generation. High overvoltage is also required for water electrolysis ($2H_2O \rightarrow 2H_2 + O_2$, $\Delta E^o = 1.23$ V) owing to the slow kinetics of proton-coupled multielectron transfer in water oxidation. Photoelectrochemical (PEC) water splitting into H_2 and O_2 might be a competitively priced technique to convert solar energy into fuels on a large production scale (Figure 1a).[3-6] The key component is the development of low-cost photoanodes for water oxidation to evolve O_2.

PEC H_2 production facilities require long sunshine hours and vast land, but there is a concern regarding the water supply in arid areas such as deserts. It is considered that the use of water vapor on the sea at high relative humidity can solve the problem of water resources in solar water splitting.[7-10] When gaseous water in the air is used, it is not necessary to purify the seawater by removing salt and impurities, which corrode the apparatuses and form by-products. Furthermore, no liquid transport system is required because water vapor is supplied by natural convection of the air over the sea.

Prototype vapor-fed PEC cells for water splitting have been investigated using an O_2-evolving photoanode, an H_2-evolving cathode, and a proton exchange membrane (PEM) as a solid polymer electrolyte (Figure 1b).[10-18] Unlike the powdered photocatalyst system, the PEC system can separate the H_2 evolved on the cathode from the O_2 evolved on the photoanode using a membrane with low permeation rates of the gases.[19, 20] In an all-solid PEM-PEC system designed for a gaseous condition, we have found that the photocurrent response was drastically enhanced by the coating of a Nafion perfluorosulfonic acid ionomer on the macroporous photoanodes owing to the increase of proton conductivity and hygroscopic property.[14-16, 21]

The PEM-PEC cell using the TiO_2 photoanodes and a carbon black-supported platinum catalyst (Pt/CB) cathode, both of which are wrapped with the proton-conducting Nafion ionomer, can evolve H_2 with 100% Faraday efficiency (FE) from water vapor as a hydrogen source.[14, 15] The Nafion ionomer-coated anatase TiO_2 nanotube array (TNTA) achieved an H_2 production rate of 600 μmol min^{-1} with an incident photon-to-current conversion efficiency (IPCE) of 16% at an applied voltage (ΔE) of 1.2 V under 365-nm ultraviolet (UV) irradiation.[14] For a

[a] Department of Chemical and Environmental Engineering, The University of Kitakyushu, Kitakyushu, Fukuoka 808-0135, Japan
[b] Precursory Research for Embryonic Science and Technology (PRESTO), Japan Science and Technology Agency (JST), Kawaguchi, Saitama 332-0012, Japan
[c] Department of Materials Molecular Science, Institute for Molecular Science, Okazaki, Aichi 444-8585, Japan
Electronic Supplementary Information (ESI) available. See DOI: 10.1039/x0xx00000x

rutile TiO_2 thin layer electrode, H_2 was evolved at 330 μmol h^{-1} (IPCE = 9%) under 385-nm irradiation.[15] However, the PEM-PEC cell using TiO_2 photoanodes requires relatively high ΔE, which is the potential difference between the photoanode and the cathode. We also confirmed that the FE of O_2 evolution was slightly lower than 100% and CO_2 was generated on the TiO_2 photoanodes.[14, 15] The CO_2 evolution is assignable to the undesired oxidation of the Nafion ionomer coating on the photoanode surface.

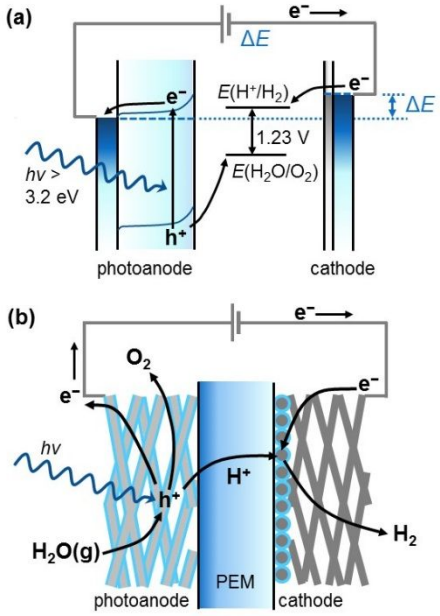

Figure 1. Schematic illustration of (a) photoelectrochemical (PEC) water splitting using an n-type semiconductor electrode as an O_2-evolving photoanode and (b) PEC system for water vapor splitting using a macroporous photoanode, a proton exchange membrane (PEM) as a solid polymer electrolyte, and a macroporous gas-diffusion cathode.

In this study, we focused on strontium titanate ($SrTiO_3$) as a photoanode in the PEM-PEC system. $SrTiO_3$ is a photocatalyst for overall water splitting into H_2 and O_2.[22-24] It is also used as a host material for visible-light-driven photocatalysts.[25-27] The conduction band minimum of $SrTiO_3$ is suitable for H_2 evolution because the flat band potential (E_{fb}) is 0.25–0.30 V more cathodic than that of rutile TiO_2 and anatase TiO_2 (see Figure S1 in Supporting Information).[28-31] The cathodic shift of E_{fb} may lead to a negative shift of the onset potential (E_{onset}) of the photoanodic current. Therefore, the ΔE for PEC water splitting by using $SrTiO_3$ photoanodes is expected to decrease. We also consider that the $SrTiO_3$ photoanode may show different photocatalytic properties for the undesired oxidation of the Nafion ionomer coating on the surface because it has been reported that the photocatalytic behavior of $SrTiO_3$ is different from that of TiO_2.[32, 33]

The aim of this study was to demonstrate the potential of a PEM-PEC cell for water vapor splitting at low ΔE without degradation of the Nafion ionomer, which is essential for fabricating a gas–electrolyte–semiconductor interface on the photoanode for gaseous conditions.[14-16] For this study, we prepared a macroporous $SrTiO_3$ photoanode by hydrothermal treatment of an anatase TNTA layer decorated on a Ti microfiber felt, which was used as a gas-diffusion conductive substrate. The PEC properties of the TNTA and $SrTiO_3$ photoanodes were compared both in liquid aqueous electrolyte and in gaseous conditions with the Nafion ionomer as a solid polymer electrolyte. We applied the ionomer-coated photoanodes to vapor-fed photoelectrolysis of water to investigate the characteristics of the macroporous $SrTiO_3$ photoanodes in the developed PEM-PEC cell in the fully gaseous condition.

Results and discussion

A Ti microfiber felt (thickness 0.1 mm, weight 15 mg cm^{-2}, porosity 66.7%)[34] was used for a gas-diffusion conductive substrate to fabricate macroporous electrodes of TNTA and $SrTiO_3$ layers. The calculated specific surface area (S_{cal}) of the Ti microfiber was 444 cm^2 g^{-1}, assuming a prismatic fiber with a 20-μm diameter from the density of hexagonal α-Ti (4.51 g cm^{-3}). The S_{cal} is much higher than that of a two-dimensional dense Ti substrate with the same thickness (45.3 cm^2 g^{-1}). The interface area between the substrate and the oxide layer should be large to effectively collect the photoexcited electrons (e^-) generated in the photoanode. We fabricated an amorphous TNTA layer by electrochemical anodization of the Ti microfiber felt in ethylene glycol with ammonium fluoride (NH_4F) at 50 V for 3 h.[14, 35] The following annealing was performed in air at 550 °C for 1 h to crystallize TiO_2 into anatase phase. The obtained anatase TNTA microfiber, which is denoted as TNTA-550 (Figure 2a), was hydrothermally treated in aqueous strontium hydroxide ($Sr(OH)_2$) at 150 °C for 2 h to convert the anatase TiO_2 into the $SrTiO_3$ phase.[36] The hydrothermally-treated sample, which is denoted as STO-hyd, was annealed in the air for 1 h at different temperatures (250–650 °C).

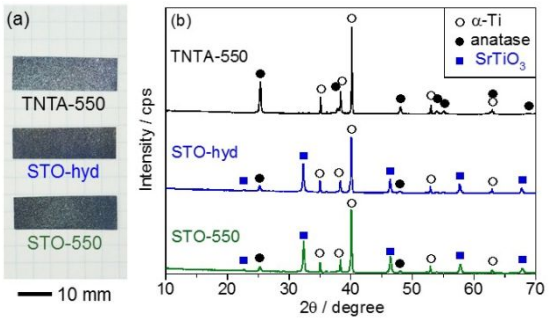

Figure 2. (a) Photos and (b) XRD patterns of the Ti microfiber after anodization in fluoride electrolyte and calcination at 550 °C for 1 h (TNTA-550), sample after hydrothermal treatment of TNTA in 25 mmol L^{-1} $Sr(OH)_2$ solution at 150 °C for 2 h (STO-hyd), and sample after calcination of STO-hyd at 550 °C for 1 h (STO-550).

Figure 2b shows X-ray diffraction (XRD) patterns of the prepared microfiber felt samples. STO-550 is the sample annealed at 550 °C. TNTA-550 contains anatase TiO_2 (PDF #00-021-1272) in addition to hexagonal α-Ti (PDF #00-044-1294) of the substrate. The hydrothermal treatment decreased the intensity of anatase peaks and generated the peaks assigned to $SrTiO_3$ (PDF #01-070-8508). The intensity of anatase TiO_2 in STO-hyd indicates that about 75% of anatase TiO_2 was transformed

into $SrTiO_3$ by the hydrothermal reaction. The crystalline phase of STO-hyd was not significantly changed by annealing at 550 °C.

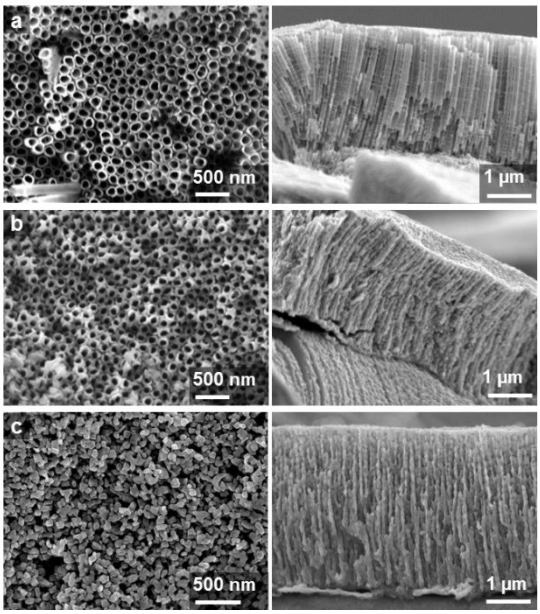

Figure 3. SEM images of surface layers decorated on the Ti microfiber of (a) TNTA-550, (b) STO-hyd, and (c) STO-550. The left side and right side show the top-view images and cross-sectional side-view images of surface layers, respectively.

Figure 3 shows SEM images of the anatase TiO_2 and $SrTiO_3$ layers on the Ti microfiber substrate. For TNTA-550, the surface of the microfibers was covered by TiO_2 nanotubes with pore sizes of about 100 nm and wall thicknesses of about 20 nm.[14] The length of the TNTA layer was 3–4 μm. STO-hyd also showed a tube-like structure even after the formation of the $SrTiO_3$ crystalline phase. In contrast, calcination at 550 °C collapsed the structure into nanocrystalline particles with an average diameter of 60 nm on top and larger sizes inside the layers. The nanoparticles were vertically connected to each other to form columnar-like structures in the $SrTiO_3$ layers. Such an interconnected pathway would facilitate the transport of the photoexcited e^- to the conductive substrate in n-type semiconductor electrodes.[35]

The SEM images of STO-550 show that the fibrous macrostructure remained after the hydrothermal treatment and the subsequent calcination (Figure 4). The microfibers were uniformly decorated by the $SrTiO_3$ layers, but there were large cracks in the long axis direction. The cracks were formed on the corner of the square cross-section of the Ti microfiber. The cut surface of the microfiber demonstrates that the $SrTiO_3$ layers were vertically grown on the flat side of the prismatic-structure substrate. The average diameter of the microfibers was expanded from the original 21 ± 2 μm to 25 ± 3 μm owing to the growth of the oxide layers with interparticle voids.

The Brunauer–Emmett–Teller (BET) specific surface area (S_{BET}) was obtained from nitrogen (N_2) adsorption isotherm measurement. The S_{BET} of TNTA-550, STO-hyd, and STO-550 was 4.5 $m^2\ g^{-1}$, 1.4 $m^2\ g^{-1}$, and 1.6 $m^2\ g^{-1}$, respectively. The measured S_{BET} was derived from the oxide layers and the Ti microfiber substrate, but the S_{cal} of Ti microfiber (0.04 $m^2\ g^{-1}$) was very low and below the limit of the quantification. The loading amount and S_{BET} of the TiO_2 layers in TNTA-550 were estimated to be 12 wt% and 37 $m^2\ g^{-1}$, which well agreed with the reported S_{BET} values of TNTA (35–40 $m^2\ g^{-1}$).[37, 38] We found that the S_{BET} was decreased by the formation of the $SrTiO_3$ crystalline phase. The S_{cal} of spherical $SrTiO_3$ particles with a diameter (D) is calculated from equation (1) using the density (ρ = 5.12 g cm^{-3}).

$$S_{cal} = 6/(D \times \rho). \quad (1)$$

The S_{BET} of the $SrTiO_3$ layers was roughly estimated from the S_{BET} of STO-550 and the loading amount of the oxide layers to be 7.3 $m^2\ g^{-1}$, which corresponds to spherical particles of D = 160 nm.

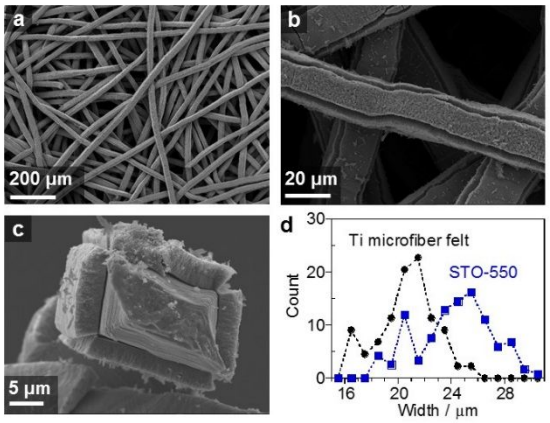

Figure 4. SEM images of STO-550: (a) macroporous structure, (b) microfiber surface, and (c) cross-section of a microfiber. (d) Distribution of the width of microfibers observed by SEM images of Ti microfiber felt and STO-550.

The PEC properties were investigated in an aqueous electrolyte solution (pH 6.7 buffer) in a conventional three-electrode configuration (see Figure S2). A silver/silver chloride electrode (Ag/AgCl, 0.195 V vs. the standard hydrogen electrode (SHE)) was used as a reference electrode. Figure 5 shows the PEC performances of the electrodes in the aqueous electrolyte under UV-LED irradiation (central wavelength λ = 365 nm, see Figure S3). The cyclic voltammograms showed an anodic photoresponse, which is typical behavior for n-type semiconductor electrodes and was attributed to the current flow of photoexcited e^- of the conduction band (CB). The anodic current was attributable to the consumption of photogenerated holes (h^+) in the valence band (VB) by water oxidation. The photocurrent density (J_{photo}) was saturated at higher anodic potentials indicating the upper limit of the IPCE.

We evaluated the E_{onset} of the photoanodic current in the backward scan. The E_{onset} of STO-hyd was decreased by 0.2 V after calcination at 550 °C. From a thermodynamic point of view, the E_{onset} of the photoanode is decreased by the cathodic shift of E_{fb}. However, the E_{fb} of STO-hyd and STO-550 are constant because the calcination did not change the $SrTiO_3$ crystalline phase (Figure 2b). In general, it is rare to observe a clear relationship between the E_{fb} and the E_{onset}, particularly for polycrystalline photoanode materials. Therefore, the negative shift of E_{onset} by calcination is explained by the increase of the crystallinity of $SrTiO_3$ layers, which decreased the recombination sites. Note that it was difficult to reliably

measure E_{fb} of the samples by Mott-Schottky analysis owing to the presence of large capacitance at around the E_{fb} (see Figure S4). An important point is that the calcination at 550 °C decreased the cathodic current of STO-hyd in the dark, which was assignable to the e^- accumulation in the oxide layers rather than H_2 evolution. The cathodic J_{photo} observed in the reverse scan was also decreased by the calcination. These cathodic currents are considered to promote the recombination loss of the photogenerated h^+ in STO-hyd at low anodic bias. Therefore, the high crystallinity of the $SrTiO_3$ layers is necessary to reduce the recombination of photogenerated h^+ by the reverse charge flow at near E_{fb}, where the electric field of the space charge layer is weak.

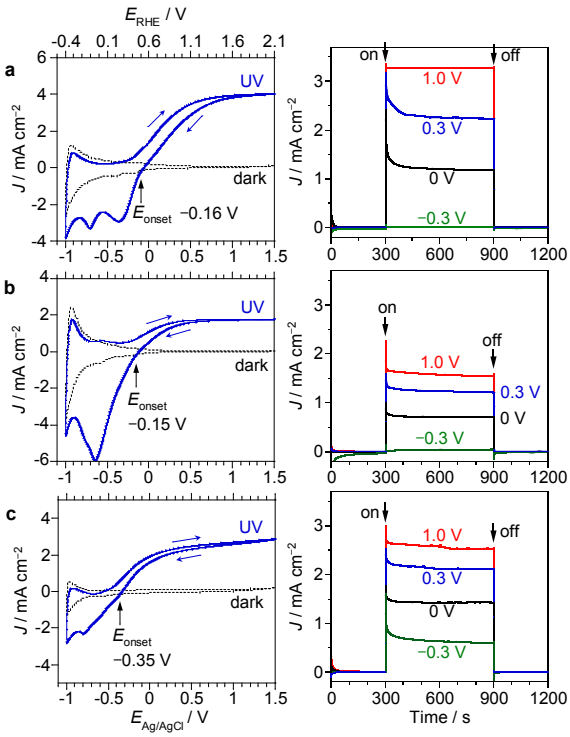

Figure 5. PEC properties of (a) TNTA-550, (b) STO-hyd, and (c) STO-550 in an aqueous Na_2SO_4 solution with phosphate buffer (pH 6.7) under dark and 365-nm UV (40 mW cm^{-2}). Left-side figures are cyclic voltammograms at a sweep rate of 50 mV s^{-1}. Right-side figures show the current density (J)–time curves at different applied potentials ($E_{Ag/AgCl}$ = −0.3, 0, 0.3, and 1.0 V).

The steady-state photocurrent response was investigated in chronoamperometry at different electrode potentials. The J_{photo} at $E_{Ag/AgCl}$ = −0.3 V was clearly observed for STO-550, but negligible for TNTA-550 and STO-hyd. In contrast to STO-550, small cathodic currents were observed for TNTA-550 and STO-hyd in the dark (Figure S5, the enlargement of the J–time curves at $E_{Ag/AgCl}$ = −0.3 V). The cathodic current, which is the charge flow in the opposite direction to the flow of photoexcited e^-, promoted the recombination loss of the photogenerated h^+, suggesting the negligible J_{photo} of STO-hyd at −0.3 V. However, the absence of the dark cathodic current explains the significant J_{photo} of STO-550 at low anodic bias.

Figure 6a summarizes the effects of the applied potential on the IPCE, which is calculated from the steady-state J_{photo} [mA cm^{-2}] and the incident light intensity (I_0 [mW cm^{-2}]) using equation (2).

$$IPCE = (1240/\lambda\ [nm]) \times J_{photo} / I_0. \quad (2)$$

The potential vs. reversible hydrogen electrode (E_{RHE}) can be obtained using the Nernst relationship between pH and the potential vs. Ag/AgCl ($E_{Ag/AgCl}$) by equation (3).

$$E_{RHE} = E_{Ag/AgCl} + 0.059\ pH + 0.195. \quad (3)$$

The IPCE of STO-550 was superior to that of TNTA-550 at low E_{RHE}. The steady-state E_{onset} (V vs. RHE) was estimated to be 0.05 V for STO-550 and 0.25 V for TNTA-550 and STO-hyd by extrapolation. The IPCE of STO-550 monotonically increased with an increase in the E_{RHE} and saturated at $E_{RHE} \geq 0.9$ V. This saturation was not due to the mass transfer limitation since the J_{photo} was increased with an increase in I_0.

Figure 6b shows the effect of calcination temperature on the IPCE of STO-hyd at different E_{RHE} (see Figure S6, steady-state photocurrent response). The best calcination temperature range was 450 °C–550 °C, and calcination at 650 °C decreased the IPCE. The analysis of the XRD patterns indicated that the normalized peak area of $SrTiO_3$ was maximized at 450 °C, but the difference was too small to explain the performance difference (see Figure S7). SEM observation showed the gradual change of the tube-like structure to the particulate structure with an increase in the calcination temperature (see Figure S8). The photocurrent response at E_{RHE} = 0.3 V was confirmed only for the STO samples with the interconnected nanocrystalline structure providing good e^- transport pathways. It is suggested that the high crystallinity and the interconnected structure are important factors for the J_{photo} of STO-550 at low anodic bias.

Figure 6c shows the action spectra of the IPCE measured under monochromatic light irradiation with different λ. A photocurrent response was clearly observed at λ = 380 nm for both TNTA-550 and STO-550. The IPCE values of STO-550 were lower than that of TNTA-550 in the whole λ at E_{RHE} = 0.9 V. In contrast, there was not a significant difference at E_{RHE} = 0.6 V. The IPCE of STO-550 was maximized at λ = 365 nm and the value (23.3%) was higher than that of TNTA-550 (16.6%) at E_{RHE} = 0.6 V. The IPCE values of $SrTiO_3$ photoanode become lower as the irradiation wavelength became shorter. This behavior was not fully understood, but it might be related to the electronic structure of $SrTiO_3$. The band gap energy (E_g) of $SrTiO_3$ is 3.25 eV (~380 nm) for indirect transition and 3.75 eV (~330 nm) for direct transition.[39]

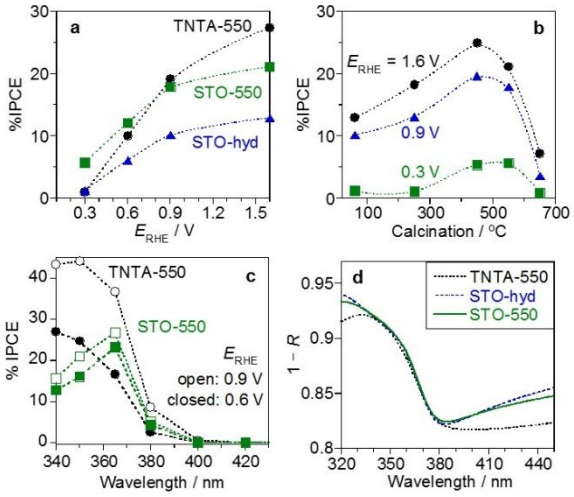

Figure 6. (a) IPCE of TNTA-550, STO-hyd, and STO-550 at different E_{RHE} and (b) effect of calcination temperature on the IPCE of STO samples under 365-nm UV (I_0 = 40 mW cm^{-2}). (c) Action spectra of (circle) TNTA-550 and (square) STO-550 at E_{RHE} = 0.6 and 0.9 V (I_0 < 1 mW cm^{-2}). (d) Diffuse reflectance UV-vis spectra of TNTA-550, STO-hyd, and STO-550. The IPCE of (a–c) was obtained in an aqueous electrolyte (pH 6.7).

Figure 6d shows the diffuse reflectance UV-vis spectra of the sample layers on microfiber felts. The photoabsorption edge was located at around 380 nm and very consistent with the λ of the photocurrent response in the action spectra. This indicates that the J_{photo} is generated by the interband transition of e^- from the VB to the CB. The optical E_g calculated from the relative reflectance (R) was found to be about 3.2 eV (see Figure S9, Tauc plot for indirect transition), which agreed with the reported E_g of anatase TiO_2 and $SrTiO_3$.[29, 30]

The oxide layers on Ti microfibers were applied to a photoanode in a vapor-fed PEC system. We fabricated membrane electrode assemblies (MEAs) using the macroporous photoanode, a Nafion N117 membrane as a PEM, and a film of Pt/CB catalyst mixed with Nafion ionomer as an H_2-evolving cathode (see Figure S10). The fabricated MEA was installed in an H-type dual-compartment glass reactor (irradiation area 1 cm^2, see Figure S11). The PEC properties were investigated under a continuous flow of argon (Ar) with water vapor (3 vol%, relative humidity > 90%) at room temperature under atmospheric pressure. There was no chemical potential difference between the photoanode and cathode compartments. We also confirmed visually that there was no droplet of liquid water on the MEA in the glass reactor.

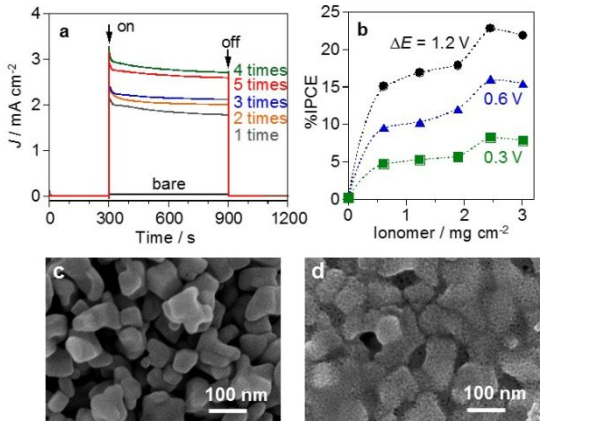

Figure 7. Photocurrent response of an STO-550|PEM|Pt/CB system under continuous Ar flow (20 mL min^{-1}) with 3 vol% water vapor at ΔE = 1.2 V under 365-nm UV (I_0 = 43 mW cm^{-2}, area 1 cm^2). (a) Effect of Nafion ionomer coating number and (b) IPCE at different ΔE as a function of the ionomer loading. SEM images of (c) bare STO-550 and (d) the STO-550 coated with Nafion ionomer four times.

Figure 7a shows the photocurrent response of STO-550 attached on a Nafion membrane in the humidified argon under UV (λ = 365 nm) at ΔE = 1.2 V. The J_{photo} of bare STO-550 was very low in the gaseous condition, suggesting the slow kinetics of water oxidation in the absence of an aqueous electrolyte. This indicates that the reaction under the water vapor environment is totally different from the conventional liquid-phase reaction. In contrast, the J_{photo} was drastically increased by the coating of Nafion ionomer thin film, which was prepared by drop cast of each 5.0 µL cm^{-2} of 5wt% ionomer dispersion on the front and back sides of the $SrTiO_3$ layers on the Ti microfiber felt. Figure 7b summarizes the effect of the ionomer loading on the IPCE of STO-550 after the coating treatment, which was repeated several times through a drying process. The IPCE was drastically increased by the first coating (0.4 mg cm^{-2}) and saturated at high loading (2.4 mg cm^{-2}) at each ΔE. The IPCE in the gas-phase condition (5%–8% at ΔE = 0.3 V) was similar to that of bare STO-550 in an aqueous electrolyte (5.7% at E_{RHE} = 0.3 V, Figure 6). This indicates that water supply as a reaction substrate is sufficiently achieved under the flow of 3 vol% water vapor for the ionomer-coated STO-550. The proton-coupled multielectron transfer in the completely gaseous condition is accelerated by the Nafion ionomer coating, which plays the role of the electrolyte. The gas-permeable ionomer thin film coated on the semiconductor surface forms a triple-phase boundary for the vapor-fed PEC reactions. As a result, the PEC performance of the ionomer-coated STO-550 under the gaseous environment was comparable to that of STO-550 in aqueous electrolyte. The Nafion ionomer thin films were observed by SEM after gold sputtering treatment to suppress the charge up during the observation (Figure S12). We confirmed that the surface of $SrTiO_3$ nanoparticles was enwrapped in the ionomer thin films (Figure 7c and 7d). Energy-dispersive X-ray spectrometer (EDS) elemental mapping images revealed that some ionomers were segregated in the void spaces and the middle part of the microfiber felt after coating four times (Figure S13 and S14). Therefore, the thickness of the ionomer thin film is difficult to estimate, but is roughly 8 nm assuming

that a coating of Nafion (1.98 g cm^{-3}) covers the surface of the oxide layer uniformly and completely.

The Nafion ionomer absorbing water increases the proton conductivity on the macroporous $SrTiO_3$ photoanode. Figure 8a shows diffuse reflectance infrared (IR) spectra of $SrTiO_3$ powders under different water vapor pressures, $P(H_2O)$. IR absorption of the adsorbed water was observed in the regions of the water bending mode (1580–2200 cm^{-1}) and hydroxyl group stretching mode (2500–3800 cm^{-1}). A band at 1640 cm^{-1} and a broad band at 2900–3650 cm^{-1} are attributed to liquid-like water layers $(H_2O)_n$ adsorbed on the oxide surface.[40, 41]

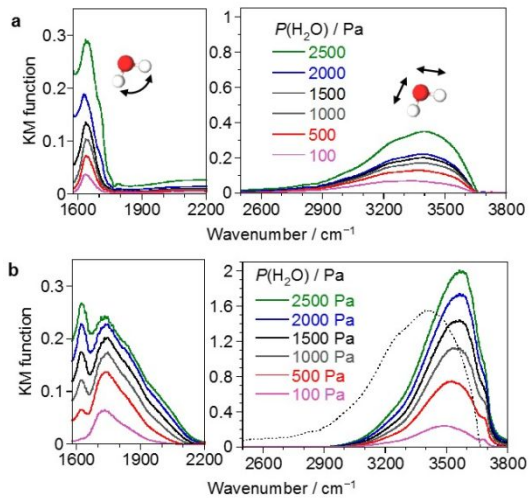

Figure 8. Diffuse reflectance IR spectra of (a) bare $SrTiO_3$ powder and (b) the $SrTiO_3$ powder mixed with a Nafion ionomer (50:50 wt%) at different water-vapor pressures, $P(H_2O)$ = 100–2500 Pa. Left-side and right-side figures show the region of the bending mode and OH stretching mode of water. The dashed curve shows the spectrum of liquid-like water adsorbate (difference spectrum of bare $SrTiO_3$ between 2000 and 2500 Pa).

Figure 8b shows the $P(H_2O)$-dependent IR spectra of the $SrTiO_3$ powder mixed with the Nafion ionomer. A broad band at 1740 cm^{-1} and a broad band at 3000–3750 cm^{-1} appeared at $P(H_2O)$ = 100 Pa. The band at 1740 cm^{-1} was attributed to the bending mode of water molecules of hydrated hydronium ions, $(H_3O^+)(H_2O)_n$.[42-44] The growth of the bending band at 1740 cm^{-1} with an increase of $P(H_2O)$ was accompanied by a band at 1620 cm^{-1} assigned to water layers, which form channels of weakly hydrogen-bonded water adsorbates to increase the proton conductivity.[44] Another feature of the weak hydrogen-bond network was observed in the OH stretching region. The broad OH stretching band was shifted to higher wavenumbers compared with the case of liquid-like water layers adsorbed on the bare $SrTiO_3$. The observed blue shift suggests that the hydrogen bonds of the water adsorbed on the ionomer-coated $SrTiO_3$ are substantially weaker than that of liquid-like water layers.[40, 41] Therefore, the hydrogen bonds of the water molecules interacting with the Nafion ionomer are significantly different from the intermolecular interaction in liquid-like water layers. A weak sharp shoulder at 3685 cm^{-1} observed for the ionomer-coated $SrTiO_3$ also indicates the presence of a "free" OH group not involved in the hydrogen bonds.[41]

The integrated IR absorption intensities of the water adsorbed on the ionomer-coated $SrTiO_3$ were much higher than those on the bare $SrTiO_3$, indicating that the coated ionomer enhances water adsorption on the surface even at low $P(H_2O)$. The Nafion ionomer exhibits a hygroscopic nature enabling it to adsorb low-concentration water vapor in the gas phase. This property would be very important in a PEM-PEC system operated in the low humidity conditions.

We performed PEC water splitting using a planar-type dual-compartment stainless-steel reactor with a UV irradiation area of 2.0 cm^2 by dosing water vapor (see Figure S15). The Ti microfibers decorated with oxide layers were used for the photoanode after the fourth coating of the Nafion ionomer (loading 2.4 mg cm^{-2}). Figure 9 shows the results of the ionomer-coated TiO_2 and $SrTiO_3$ electrodes in the vapor-fed PEC system at different ΔE. The photocurrent was initially overshot and decreased to the steady value when ΔE was low. The J_{photo} of STO-550 was higher than that of TNTA-550 at $\Delta E \geq 0.3$ V. The cyclic voltammograms show that the ΔE_{onset} of STO-550 is less than that of TNTA-550 (see Figure S16) as discussed earlier.

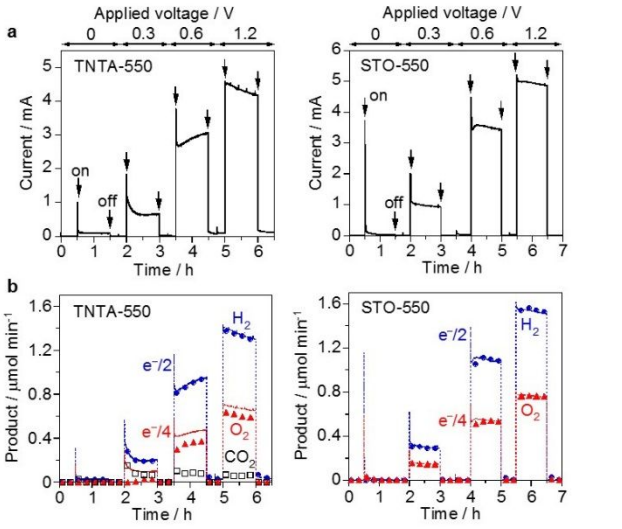

Figure 9. Vapor-fed photoelectrolysis of water by an ionomer-coated photoanode | PEM | Pt/CB under 365 nm UV (I_0 = 42 mW cm^{-2}, area 2 cm^2) at different external voltages. The photoanode was TNTA-550 and STO-550. (a) Photocurrent response and (b) formation rate of H_2 (circle) in the cathode compartment and O_2 (triangle) and CO_2 (square) in the photoanode compartment.

Figure 9b shows the formation rates of gasses in the PEM-PEC cell analyzed by gas chromatography. The two compartments of the cell were separated by the Nafion membrane sandwiched by a photoanode and a cathode. At $\Delta E \geq 0.3$ V, the H_2 evolution rate in the cathode compartment was consistent with half of the charge flow ($e^-/2$) passing through the outer circuit. This indicates that the two-electron reduction ($2H^+ + 2e^- \rightarrow H_2$) is promoted on the ionomer-coated Pt/CB catalyst. In the photoanode compartment, CO_2 was evolved in addition to O_2 for the ionomer-coated TNTA-550, but the CO_2 was below the limit of quantification for the ionomer-coated STO-550. We found that the four-electron oxidation of water ($2H_2O + 4h^+ \rightarrow O_2 + 4H^+$) was promoted over the $SrTiO_3$

photoanode at $\Delta E \geq 0.3$ V because the O_2 evolution rate was consistent with one-quarter of the charge flow ($e^-/4$). Overall water splitting was proved by the ratio of 2:1 for H_2 and O_2 evolutions in the vapor-fed PEM-PEC cell using the $SrTiO_3$ photoanode at $\Delta E = 0.3$ V (see Figure S17). In the case of TNTA, H_2 was evolved even at $\Delta E = 0$ V as previously reported.[14, 17] However, the H_2 evolution was not necessarily derived from overall water splitting because the major product was CO_2 at $\Delta E = 0.3$ V. This suggests that the coated Nafion ionomer works as a sacrificial e^- donor in the case of the J_{photo} of TNTA-550 at $\Delta E \leq 0.3$ V.

Table 1. Effect of ΔE on IPCE, Faraday efficiency, and CO_2 formation rate in vapor-fed photoelectrolysis of water over an ionomer-coated photoanode | PEM | Pt/CB under UV irradiation.[a]

Photoanode	ΔE / V	%IPCE	%FE(H_2)	%FE(O_2)	r(CO_2) [b]
TNTA-550	0.0	0.35	89.4	— [c]	n.d. [d]
	0.3	2.61	98.2	26.5	0.061
	0.6	12.1	101.3	82.0	0.081
	1.2	17.3	102.2	92.4	0.059
STO-550	0.0	0.09	—	—	n.d.
	0.3	3.90	98.7	99.3	n.d.
	0.6	14.3	101.3	99.8	n.d.
	1.2	20.2	101.0	99.8	n.d.

[*a*] λ = 365 nm, I_0 = 42 mW cm^{-2}, irradiation area 2 cm^2. [*b*] Rate of CO_2 evolution [μmol min^{-1}]. [*c*] Below limit of quantification. [*d*] Not detected.

Table 1 summarizes the IPCE and FE values in the vapor-fed PEM-PEC cell. The FE was calculated using equation (4).

$$FE = (n_e \times F \times r) / J_{photo}, \quad (4)$$

where n_e is the number of e^- required to form a product (2 for H_2 and 4 for O_2), F is the Faraday constant, and r is the rate of product formation. The IPCE of STO-550 (20.2%) was higher than that of TNATA-550 (17.3%) at ΔE =1.2 V under λ = 365 nm (42 mW cm^{-2}). In the case of the TNTA-550 photoanode, the FE of O_2 was less than 100% even at 1.2 V owing to the CO_2 formation. The oxidative decomposition of the coated ionomer into CO_2 is considered to be promoted by radical species such as a hydroxyl radical, which can be generated by one-electron oxidation of water ($H_2O + h^+ \rightarrow \bullet OH + H^+$).[45-47] When STO-550 was used as a photoanode, the FE of O_2 was almost 100% owing to the absence of CO_2 formation. The difference in the reactivity would be dependent on the surface properties of TiO_2 and $SrTiO_3$. Further study is required to elucidate the mechanism at a molecular level.

Figure 10 shows the results of the long term durability test of the PEM-PEC system. The water splitting under the vapor environment was performed using a scaled-up reactor with a UV irradiation area of 16 cm^2 (see Figure S18). The photocurrent of the ionomer-coated TNTA-550 was gradually decreased with the PEC operation time. In contrast, the photocurrent was relatively constant when the ionomer-coated STO-550 was used as a photoanode. The IPCE after the 10-h PEC reaction was 15.5% and 6.3% for STO-550 and TNTA-550, respectively. In the case of TNTA-550, the O_2 evolution rate was lower than $e^-/4$ owing to the formation of CO_2. The CO_2 evolution rate gradually decreased, but the photocurrent was also decreased. For STO-550, the O_2 evolution rate was almost consistent with $e^-/4$, but a small amount of CO_2 formation was observed in this large scale cell. However, the photocurrent of STO-550 was more stable than the case of TNTA-550. We also confirmed that the PEC water splitting is induced even when the water vapor concentration is 1.4 vol% (relative humidity ~45%) (Figure S19).

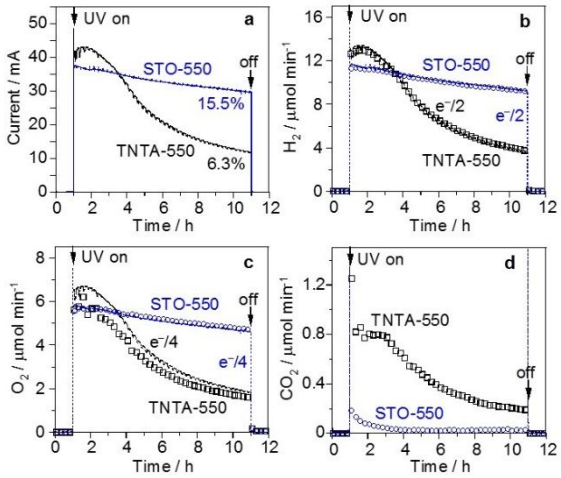

Figure 10. Photoelectrolysis under 3 vol% water vapor by ionomer-coated photoanode | PEM | Pt/CB at 1.2 V with 365-nm UV irradiation (I_0 = 40 mW cm^{-2}, area 16 cm^2). The photoanode was STO-550 and TNTA-550. (a) Photocurrent response. (b) H_2 formation rate in the cathode compartment and the flow rate of charge divided by 2 ($e^-/2$). The formation rate of (c) O_2 and (d) CO_2 in the photoanode compartment and $e^-/4$.

We performed EDS elemental analysis of the photoanodes after the PEC reaction (Table 2). The decrease of the atomic percentages of carbon and fluorine on the ionomer-coated TNTA-550 indicated the degradation of the coated Nafion ionomer during the PEC reaction. The removal of the Nafion ionomer from the TNTA-550 surface was confirmed by the EDS elemental mapping image (Figure S20). Similar behavior was observed for the rutile TiO_2 electrode during the PEC water splitting under vapor stream.[15] However, there was no significant change for the ionomer-coated STO-550 electrodes before and after the vapor-fed photoelectrolysis of water. The durability of the PEM-PEC system under the water vapor environment was improved by the use of $SrTiO_3$ instead of TiO_2 as the photoanode. The photogenerated h^+ in VB of $SrTiO_3$ were selectively used for the four-electron oxidation of water to evolve O_2 instead of forming radical species to decompose the ionomer. The suppression of CO_2 formation resulted in improved durability of the PEM-PEC system under UV irradiation.

Table 2. EDS elemental analysis (atomic percentages) of the ionomer-coated photoanodes before and after vapor-fed photoelectrolysis of water. [a]

Photoanode	Reaction	Sr	Ti	O	C	F
TNTA-550	0 h	0	19.3	35.1	14.1	31.6
	10 h	0	28.6	51.3	8.44	11.7
STO-550	0 h	6.2	9.1	24.5	26.9	33.4
	10 h	5.5	9.2	24.2	26.1	35.1

[*a*] The reaction condition is the same as that in Figure 10.

Finally, we investigated the effect of light intensity on the photocurrent response (Figure 11). When the I_0 of UV LED was increased step by step, the J_{photo} of STO-550 was monotonically increased, but the J_{photo} of TNTA-550 was saturated at around I_0 = 60 mW cm^{-2}. As a result, the IPCE of TNTA-550 was drastically decreased with an increase in I_0. This is contrary to STO-550, which exhibited a relatively high IPCE even under high I_0 where a large number of photoexcited e^- and h^+ were generated. The high IPCE even under high I_0 suggests the fast kinetics of water oxidation to evolve O_2 on the $SrTiO_3$ surface. The high selectivity of O_2 evolution is also explained by the fast kinetics of the proton-coupled multielectron transfer process because the water oxidation intermediates might be a reactive species to promote undesired oxidation of the Nafion ionomer. Investigation of the reaction mechanism is planned for further understanding the specific properties of the $SrTiO_3$ surface for water oxidation, high selectivity and fast kinetics of O_2 evolution.

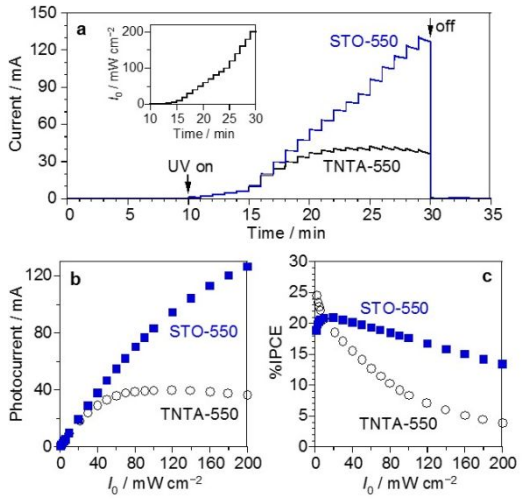

Figure 11. Effect of incident light intensity (I_0) on the photocurrent response of the ionomer-coated photoanodes (STO-550 and TNTA-550) in the vapor-fed PEM-PEC system at ΔE = 1.2 V under 365-nm UV (irradiation area 16 cm²). (a) Photocurrent response by a step-by-step increase of I_0 up to 200 mW cm^{-2} (see inset). (b) Relationship between the photocurrent and I_0. (c) Dependence of IPCE on I_0.

In this study, we have succeeded in developing a vapor-fed PEM-PEC system for overall water splitting at a low electric bias of ΔE = 0.3 V. The results provided information to facilitate the design of photoanodes for the PEM-PEC system: 1) E_{onset} of photocurrent response can be shifted to a negative direction using an n-type semiconductor with a high energy level (more negative) E_{fb}, high crystallinity, and the interconnected nanocrystalline structure, 2) The reaction selectivity of the photogenerated h^+ on the photoanode surface affects not only the Faraday efficiency of O_2 evolution but also the long-term stability of the Nafion ionomer-coated photoanode in the PEM-PEC system, 3) The Nafion ionomer thin films efficiently absorb water molecules under the gas environment, 4) The $SrTiO_3$ photoanode has good photocurrent response even under high I_0, suggesting the fast kinetics of proton-coupled multielectron transfer from water adsorbate. For further development, we have to use solar energy more efficiently by using narrow gap materials, which should exhibit a high energy level E_{fb}, high charge separation at a low electric field, and high selectivity for O_2 evolution. One candidate is visible-light-sensitized $SrTiO_3$, which can be synthesized by metal cation doping.[25-27]

Experimental

Preparation of oxide-decorated Ti microfiber felts

Sintered Ti microfiber felt (Nikko Techno, Japan) was cleaned in acetone and deionized water before electrochemical anodization to prepare TNTA on the Ti microfibers. The anodization was performed in a two-electrode system at ΔE = 50 V for 3 h at 20 °C. The electrolyte solution was composed of ethylene glycol (99.5%, Wako Pure Chemicals, Japan), 0.25 wt% NH_4F (97%, Wako Pure Chemicals), and 10 vol% H_2O. The obtained TNTA layer on the Ti microfiber felt was washed with water, dried at 80 °C, and calcined in the air at 550 °C for 1 h to obtain the anatase sample called TNTA-550.

The TNTA-550 was treated in an aqueous solution of 25 mmol L^{-1} $Sr(OH)_2$ at the hydrothermal condition. The solution was prepared by dissolving 0.5 g of $Sr(OH)_2{\cdot}8H_2O$ (90%, Wako Pure Chemicals) in 80 mL deionized water. The TNTA-550 was soaked in the solution and maintained in a polytetrafluoroethylene-lined autoclave under auto-generated pressure at 150 °C for 2 h. After the hydrothermal reaction, the sample was washed with water and dried at 80 °C. The obtained $SrTiO_3$ layer on Ti microfiber felt, which is denoted as STO-hyd, was calcined in the air at 250–650 °C for 1 h. The samples calcined at 550 °C are denoted as STO-550.

Nafion perfluorosulfonic acid ionomer dispersion (5 wt% in alcohol and 45 wt% water, Sigma-Aldrich Japan, Japan) was used for the coating of the macroporous electrodes. The drop cast with a coverage of 10 μL cm^{-2} (5.0 μL cm^{-2} on each of the front and back sides) was repeated several times after drying at 80 °C for 30 min.

Characterization of electrodes

XRD measurements were carried out on a SmartLab diffractometer (Rigaku, Japan) using Cu Kα radiation at 45 kV and 200 mA. Calibration curves were obtained from anatase TiO_2 and $SrTiO_3$ powders (Kojundo Chemical Laboratory, Japan). SEM images and EDS elemental analysis were recorded on JSM-7800F (JEOL, Japan) with an acceleration voltage of 10 kV. SEM images were also observed on S-5200 (Hitachi, Japan) with an acceleration voltage of 5 kV. Sputter coating of gold was applied

to the sample using an E-1010 (Hitachi) to reduce the charge-up of the Nafion ionomer. Nitrogen adsorption isotherms of the Ti microfibers decorated with oxide layers were measured at −196 °C after evacuation at 200 °C for 2 h (BELSORP-mini; Bel Japan, Japan). Diffuse reflectance UV-Vis spectrum was recorded on a UV-2600 spectrometer (Shimadzu, Japan) with an integrating sphere by using the Ti microfiber felt on barium sulfate powder as a reference.

IR spectroscopy of $SrTiO_3$ powder

Diffuse reflectance IR spectra of $SrTiO_3$ powder (Wako Pure Chemicals) were measured by an FT/IR-6600 spectrometer (JASCO, Japan) equipped with a mercury cadmium telluride (MCT) detector. The sample (20 mg) was held in a high vacuum cell equipped with a CaF_2 window. The background was taken with the sample in a vacuum (pressure < 10^{-3} Pa). The intensity of IR absorption was estimated by the Kubelka-Munk equation.

PEC measurements in aqueous electrolyte

A conventional three-electrode system consisting of an Ag/AgCl reference electrode and a platinum wire counter electrode was used in a one-compartment glass reactor. The electrode potential of the Ag/AgCl reference electrode is 0.195 V vs. SHE. The oxide-decorated Ti microfiber felt was soaked in an aqueous electrolyte solution of 0.2 mol L^{-1} sodium sulfate (Na_2SO_4) and 0.1 mol L^{-1} sodium phosphate buffer (pH 6.7). The O_2 dissolved in the electrolyte was purged by argon bubbling. The electrode potential was controlled by an ECstat-101 potentiostat (EC Frontier, Japan). Photoirradiation was performed using a 365-nm UV light-emitting diode (LED, NS365L-7SMG, Nitride Semiconductor, Japan) and a 300-W xenon lamp with bandpass filters (MAX-303, Asahi Spectra, Japan). The irradiation area was adjusted to 1.0 cm^2 by masking the electrode surface using polyimide film tapes.

Preparation of the membrane electrode assembly

A cathode film was prepared on a polytetrafluoroethylene sheet by a bar coating method using catalyst ink containing 47 wt% Pt/CB (TEC10E50E, Tanaka Kikinzoku, Japan) and Nafion ionomer (weight ratio 1:1). The Pt loading of the film was about 0.15 mg cm^{-2}. The ionomer-mixed Pt/CB film was transferred onto a Nafion membrane (thickness of 183 μm, N117, DuPont, USA) by a hot pressing method at 15 kN and 140 °C. Then, the oxide layer decorated on the Ti microfiber felt was attached to the membrane on the opposite side of the cathode by hot pressing at 10 kN and 140 °C. The prepared MEA was applied to the PEC measurements for the gas phase.

PEC measurements in the gas phase

Two-electrode systems were used in an H-type dual-compartment glass reactor (irradiation area 1.0 cm^2) and two planar-type dual-compartment stainless-steel reactors (irradiation area 2.0 and 16.0 cm^2). The fabricated MEA was sandwiched with two current collectors of a gold-coated copper plate. The current collectors exhibited square window(s) for UV irradiation. A wet-proofed Toray carbon paper (5×5 cm, Fuel Cell Store, USA) was used for a gas-diffusion layer of the ionomer-mixed Pt/CB cathode. The MEA for the H-type glass reactor was prepared at a size of 40 × 40 mm^2 for the Nafion membrane and 14 × 14 mm^2 for the electrodes. The ΔE was controlled by an ECstat-101 potentiostat and the photoirradiation was performed using an NS365L-7SMG LED. The MEAs for the planar-type stainless-steel reactors were prepared at a size of 50 × 50 mm^2 for the Nafion membrane and 20 × 20 mm^2 for the electrodes and a size of 80 × 80 mm^2 for the Nafion membrane and 50 × 50 mm^2 for the electrodes. The direct-current ΔE between the two electrodes was controlled by a VersaSTAT3 potentiostat (AMETEK, USA). Photoirradiation was performed using 365-nm UV LEDs (custom made lamp; Nitride Semiconductor).

Water vapor was introduced into each compartment by passing argon (20 mL min^{-1}) through a bubbler filled with deionized water at room temperature. The concentration of water vapor was about 3 vol% and the relative humidity was higher than 90%, which was measured by a humidity transmitter (EE33, E+E Elektronik, Austria). The H_2 in the cathode compartment was analyzed by an on-line gas chromatograph with a thermal conductivity detector (GC-TCD, GC-8A; Shimadzu) equipped with an MS-5A column of an Ar carrier. The O_2 and CO_2 in the photoanode compartments were analyzed by two GC-TCDs (GC-8A and GC-2014; Shimadzu) with an MS-5A column with an Ar carrier and Shincarbon-ST column with a He carrier.

Conclusions

Overall water splitting into H_2 and O_2 with a 2:1 ratio was achieved using Nafion ionomer-coated $SrTiO_3$ microfiber felts for an O_2 evolution photoanode in a PEM-PEC cell under water vapor environment. Vapor-fed photoelectrolysis of water was induced at ΔE = 0.3 V under UV irradiation at room temperature under atmospheric pressure (IPCE = 3.9% at λ = 365 nm, FE of H_2 and O_2 ≥ 99%). The overpotential for PEC water oxidation to evolve O_2 was cathodically shifted by using $SrTiO_3$. Calcination treatment of $SrTiO_3$ nanocrystals enhanced the J_{photo} at 0.3 V vs. RHE owing to the decrease of the recombination loss of the photogenerated carriers, which is suggested by the calcination decreasing the cathodic current at potentials less than E_{fb}. The coated ionomer was revealed to increase the water adsorption amount in the low concentration of water vapor and form hydrated hydronium ions with weakly hydrogen-bonded water molecules. The proton conductivity of the hydrated ionomer enhanced the proton-coupled multielectron transfer from the water adsorbate by the photogenerated h^+ on the photoanode surface in the gas environment.

The $SrTiO_3$ photoanode was revealed to suppress the undesired oxidation of the gas permeable ionomer thin film coated on the electrode surface, which easily occurs on TiO_2 photoanodes. Because the triple-phase boundary, which is the gas–electrolyte–semiconductor interface, is essential for the charge transfer process under the water vapor environment, the photocurrent of the PEM-PEC system using TiO_2 photoanodes gradually decreased with the degradation of the proton-conducting electrolyte thin film. On the contrary, the

vapor-fed PEM-PEC system using the $SrTiO_3$ photoanode was robust and durable (H_2 evolution rate = 550 μmol h^{-1} at ΔE = 1.2 V after a 10-h operation). The low CO_2 evolution rate indicates the high selectivity for O_2 evolution by four-electron oxidation of water layers adsorbed on a $SrTiO_3$–ionomer interface. The superior photocurrent response even under high incident UV light intensity proves the fast kinetics of water oxidation to evolve O_2 over the $SrTiO_3$ surface.

Conflicts of interest

There are no conflicts to declare.

Acknowledgments

This work was supported by the Japan Science and Technology Agency (JST), Precursory Research for Embryonic Science and Technology (PRESTO), grant number JPMJPR15S1, JPMJPR16S7, and JPMJPR18T1 and Joint Research of Institute for Molecular Science (IMS), program number 606.

References

1. N. S. Lewis and D. G. Nocera, *Proc. Natl. Acad. Sci.*, 2006, **103**, 15729-15735.
2. T. R. Cook, D. K. Dogutan, S. Y. Reece, Y. Surendranath, T. S. Teets and D. G. Nocera, *Chem. Rev.*, 2010, **110**, 6474-6502.
3. B. A. Pinaud, J. D. Benck, L. C. Seitz, A. J. Forman, Z. Chen, T. G. Deutsch, B. D. James, K. N. Baum, G. N. Baum, S. Ardo, H. Wang, E. Miller and T. F. Jaramillo, *Energy Environ. Sci.*, 2013, **6**.
4. M. G. Walter, E. L. Warren, J. R. McKone, S. W. Boettcher, Q. Mi, E. A. Santori and N. S. Lewis, *Chem. Rev.*, 2010, **110**, 6446-6473.
5. T. Hisatomi, J. Kubota and K. Domen, *Chem. Soc. Rev.*, 2014, **43**, 7520-7535.
6. C. Xiang, A. Z. Weber, S. Ardo, A. Berger, Y. Chen, R. Coridan, K. T. Fountaine, S. Haussener, S. Hu, R. Liu, N. S. Lewis, M. A. Modestino, M. M. Shaner, M. R. Singh, J. C. Stevens, K. Sun and K. Walczak, *Angew. Chem. Int. Ed. Engl.*, 2016, **55**, 12974-12988.
7. M. A. Modestino, M. Dumortier, S. M. Hosseini Hashemi, S. Haussener, C. Moser and D. Psaltis, *Lab Chip*, 2015, **15**, 2287-2296.
8. S. Kumari, R. Turner White, B. Kumar and J. M. Spurgeon, *Energy Environ. Sci.*, 2016, **9**, 1725-1733.
9. G. Heremans, C. Trompoukis, N. Daems, T. Bosserez, I. F. J. Vankelecom, J. A. Martens and J. Rongé, *Sustainable Energy Fuels*, 2017, **1**, 2061-2065.
10. J. Rongé, S. Deng, S. Pulinthanathu Sree, T. Bosserez, S. W. Verbruggen, N. Kumar Singh, J. Dendooven, M. B. J. Roeffaers, F. Taulelle, M. De Volder, C. Detavernier and J. A. Martens, *RSC Adv.*, 2014, **4**, 29286-29290.
11. J. Georgieva, S. Armyanov, I. Poulios, A. D. Jannakoudakis and S. Sotiropoulos, *Electrochem. Solid-State Lett.*, 2010, **13**, P11-P13.
12. K. O. Iwu, A. Galeckas, A. Y. Kuznetsov and T. Norby, *Electrochim. Acta*, 2013, **97**, 320-325.
13. T. Stoll, G. Zafeiropoulos and M. N. Tsampas, *Int. J. Hydrogen Energy*, 2016, **41**, 17807-17817.
14. F. Amano, H. Mukohara, A. Shintani and K. Tsurui, *ChemSusChem*, 2019, **12**, 1925-1930.
15. F. Amano, H. Mukohara, H. Sato and T. Ohno, *Sustainable Energy Fuels*, 2019, DOI: 10.1039/C9SE00292H.
16. F. Amano, A. Shintani, H. Mukohara, Y. M. Hwang and K. Tsurui, *Front. Chem.*, 2018, **6**, 598.
17. J. Rongé, D. Nijs, S. Kerkhofs, K. Masschaele and J. A. Martens, *Phys. Chem. Chem. Phys.*, 2013, **15**, 9315-9325.
18. T. Stoll, G. Zafeiropoulos, I. Dogan, H. Genuit, R. Lavrijsen, B. Koopmans and M. N. Tsampas, *Electrochem. Commun.*, 2017, **82**, 47-51.
19. A. Berger, R. A. Segalman and J. Newman, *Energy Environ. Sci.*, 2014, **7**, 1468-1476.
20. K. Xu, A. Chatzitakis, E. Vøllestad, Q. Ruan, J. Tang and T. Norby, *Int. J. Hydrogen Energy*, 2019, **44**, 587-593.
21. G. Zafeiropoulos, H. Johnson, S. Kinge, M. C. M. Van De Sanden and M. N. Tsampas, *ACS Appl. Mater. Interfaces*, 2019, **11**, 41267-41280.
22. Y. Ham, T. Hisatomi, Y. Goto, Y. Moriya, Y. Sakata, A. Yamakata, J. Kubota and K. Domen, *J. Mater. Chem. A*, 2016, **4**, 3027-3033.
23. Y. Goto, T. Hisatomi, Q. Wang, T. Higashi, K. Ishikiriyama, T. Maeda, Y. Sakata, S. Okunaka, H. Tokudome, M. Katayama, S. Akiyama, H. Nishiyama, Y. Inoue, T. Takewaki, T. Setoyama, T. Minegishi, T. Takata, T. Yamada and K. Domen, *Joule*, 2018, **2**, 509-520.
24. H. Lyu, T. Hisatomi, Y. Goto, M. Yoshida, T. Higashi, M. Katayama, T. Takata, T. Minegishi, H. Nishiyama, T. Yamada, Y. Sakata, K. Asakura and K. Domen, *Chem. Sci.*, 2019, **10**, 3196-3201.
25. R. Konta, T. Ishii, H. Kato and A. Kudo, *J. Phys. Chem. B*, 2004, **108**, 8992-8995.
26. H. Kato, Y. Sasaki, N. Shirakura and A. Kudo, *J. Mater. Chem. A*, 2013, **1**, 12327-12333.
27. Q. Wang, T. Hisatomi, S. S. K. Ma, Y. Li and K. Domen, *Chem. Mater.*, 2014, **26**, 4144-4150.
28. M. A. Butler and D. S. Ginley, *J. Electrochem. Soc.*, 1978, **125**, 228-232.
29. H. P. Maruska and A. K. Ghosh, *Sol. Energy*, 1978, **20**, 443-458.
30. L. Kavan, M. Grätzel, S. E. Gilbert, C. Klemenz and H. J. Scheel, *J. Am. Chem. Soc.*, 1996, **118**, 6716-6723.
31. W. Tadashi, F. Akira and H. Ken-ichi, *Bull. Chem. Soc. Jpn.*, 1976, **49**, 355-358.
32. M. Miyauchi, A. Nakajima, A. Fujishima, K. Hashimoto and T. Watanabe, *Chem. Mater.*, 2000, **12**, 3-5.
33. M. Miyauchi, A. Nakajima, T. Watanabe and K. Hashimoto, *Chem. Mater.*, 2002, **14**, 2812-2816.
34. F. Amano, A. Shintani, K. Tsurui and Y.-M. Hwang, *Mater. Lett.*, 2017, **199**, 68-71.
35. F. Amano, H. Mukohara and A. Shintani, *J. Electrochem. Soc.*, 2018, **165**, H3164-H3169.
36. Z. Jiao, T. Chen, J. Xiong, T. Wang, G. Lu, J. Ye and Y. Bi, *Sci. Rep.*, 2013, **3**, 2720.
37. M. Paulose, H. E. Prakasam, O. K. Varghese, L. Peng, K. C. Popat, G. K. Mor, T. A. Desai and C. A. Grimes, *J. Phys. Chem. C*, 2007, **111**, 14992-14997.
38. T. Zhang, X. Hu, M. Fang, L. Zhang and Z. Wang, *CrystEngComm*, 2012, **14**, 7656-7661.
39. K. v. Benthem, C. Elsässer and R. H. French, *J. Appl. Phys.*, 2001, **90**, 6156-6164.
40. K. Shirai, T. Sugimoto, K. Watanabe, M. Haruta, H. Kurata and Y. Matsumoto, *Nano Lett.*, 2016, **16**, 1323-1327.
41. K. Shirai, G. Fazio, T. Sugimoto, D. Selli, L. Ferraro, K. Watanabe, M. Haruta, B. Ohtani, H. Kurata, C. Di Valentin and Y. Matsumoto, *J. Am. Chem. Soc.*, 2018, **140**, 1415-1422.

42. R. Buzzoni, S. Bordiga, G. Ricchiardi, G. Spoto and A. Zecchina, *J. Phys. Chem.*, 1995, **99**, 11937-11951.
43. D. W. M. Hofmann, L. Kuleshova, B. D'Aguanno, V. Di Noto, E. Negro, F. Conti and M. Vittadello, *J. Phys. Chem. B*, 2009, **113**, 632-639.
44. K. Kunimatsu, B. Bae, K. Miyatake, H. Uchida and M. Watanabe, *J. Phys. Chem. B*, 2011, **115**, 4315-4321.
45. C. S. Turchi and D. F. Ollis, *J. Catal.*, 1990, **122**, 178-192.
46. Y. Nosaka and A. Y. Nosaka, *Chem. Rev.*, 2017, **117**, 11302-11336.
47. S. W. Verbruggen, M. Van Hal, T. Bosserez, J. Rongé, B. Hauchecorne, J. A. Martens and S. Lenaerts, *ChemSusChem*, 2017, **10**, 1413-1418.

A table of contents entry

A proton exchange membrane (PEM) system using a $SrTiO_3$ gas-diffusion photoanode achieves vapor-fed photoelectrolysis of water at an applied voltage of 0.3 V.